Bending behavior of octet-truss lattice structures: Modelling options, numerical characterization and experimental validation

N. Korshunova [a],[*], G. Alaimo [b], S.B. Hosseini [d], M. Carraturo [b], A. Reali [b], J. Niiranen [d], F. Auricchio [b], E. Rank [c], S. Kollmannsberger [a]

[a] Chair of Computational Modeling and Simulation, Technische Universität München, Germany
[b] Department of Civil Engineering and Architecture, University of Pavia, Italy
[c] Institute for Advanced Study, Technische Universität München, Germany
[d] Department of Civil Engineering, Aalto University, Finland

HIGHLIGHTS

- Process-induced defects affect the mechanical behavior of AM octet-truss lattices.
- An immersed image-based workflow efficiently incorporates as-manufactured geometries.
- CT-based numerical results show an excellent agreement with experimental data.
- A flexible framework includes high-order continuum theories to account for size effects.

GRAPHICAL ABSTRACT
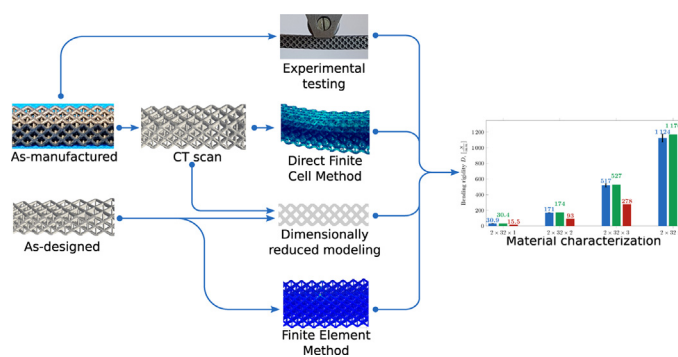
ARTICLE INFO

ABSTRACT

Selective Laser Melting (SLM) technology has undergone significant development in the past years providing unique flexibility for the fabrication of complex metamaterials such as octet-truss lattices. However, the microstructure can exhibit significant variations due to the high complexity of the manufacturing process. Consequently, the mechanical behavior, in particular, linear elastic response, of these lattices is strongly dependent on the process-induced defects, raising the importance on the incorporation of as-manufactured geometries into the computational structural analysis. This, in turn, challenges the traditional mesh-conforming methods making the computational costs prohibitively large. In the present work, an immersed image-to-analysis framework is applied to efficiently evaluate the bending behavior of AM lattices. To this end, we employ the Finite Cell Method (FCM) to perform a three-dimensional numerical analysis of the three-point bending test of a lattice structure and compare the as-designed to as-manufactured effective properties. Furthermore, we undertake a comprehensive study on the applicability of dimensionally reduced beam models to the prediction of the bending behavior of lattice beams and validate classical and strain gradient beam theories applied in combination with the FCM. The numerical findings suggest that the octet-truss lattices exhibit size effects, thus, requiring a flexible framework to incorporate high-order continuum theories.

* Corresponding author.
E-mail address: nina.korshunova@tum.de (N. Korshunova).

1. Introduction

Mechanical metamaterials have received much attention in the past decades [32,34]. One of the most common examples are octet-truss lattices. These regular, periodic structures are attractive for many industries due to the possibility of largely decoupling the effective stiffness and strength from relative density [5,29,35,47]. One further advantage of the octet-truss lattices is the possibility to relate their mechanical properties to the truss topology and geometry (see e.g. [5,21,29,37]). Although this relation facilitates their design for specific applications, some geometrical constraints push traditional manufacturing techniques of octet-truss lattices to their boundaries.

Recent developments in additive manufacturing have provided a unique possibility to produce such metamaterials at very small scales. Yet, the design freedom comes at the cost of process complexity. The process-induced features, even defects, often occur in the produced structures, especially metal lattices, thus altering the mechanical behavior of final parts [8,11,24,25,6]. Therefore, to achieve a reliable prediction of the effective properties of these imperfect structures, as-manufactured geometries should be incorporated into computer-aided engineering (CAE). One of the common ways to acquire the as-manufactured AM geometry is to perform a Computed Tomography (CT) scan [6,8,43]. The scanned images provide extensive information about the microstructure of 3D printed components up to a scan resolution in the order of few microns. Thus, the CT-based analysis could lead to a better prediction of the mechanical behavior of 3D printed structures.

In the present work, we focus on the effective linear elastic bending behavior of octet-truss lattices. The most common numerical approaches for its prediction are three-dimensional (3D) Finite Element Analyses (FEA) and the application of one-dimensional (1D) beam theories. These techniques represent the two engineering extremes: one provides the most realistic solution, while the other delivers a fast and quick approximation. 3D and 1D numerical analyses are commonly used in different areas of engineering. Each of them faces major challenges when applied to additively manufactured metamaterials.

To make CT images suitable for a traditional mesh-conforming three-dimensional analysis, geometry reconstruction and mesh generation are required [23,25,42]. These steps tend to become especially laborious when metamaterials are considered. Consequently, the numerical studies are often conducted only on some specific regions of the lattices, for example on the periodic representative volumes, or by modifying the idealized CAD models [4,22–24]. To overcome these long and tedious steps, a class of immersed domain methods has been developed. Immersed domain methods separate the geometrical representation from the applied discretization, thus, eliminating the necessity of geometry reconstruction and simplifying the mesh generation process. In the present work, the Finite Cell Method (FCM) is employed to perform numerical analysis directly on CT scan images of as-manufactured octet-truss lattices [7,31].

Concerning 1D analyses, the conventional continuum beam theories are not necessarily applicable to the evaluation of the metamaterial or effective bending behavior. They strongly rely on the assumption of the separation of scales, i.e., the microstructural characteristic length should be much smaller than the size of the representative volume element. Nevertheless, it has been determined experimentally and numerically that these components cannot be described by conventional continuum models, such as e.g. Euler-Bernoulli or Timoshenko beam theories, when the size of the periodic cell approaches the typical wavelength of the variation of the macroscopic

mechanical fields. Such deviations are normally referred to as size effects. These effects can arise at different scales. When lattice or foam-like structures are considered, size effects can occur at the scale of millimeters [30]. If this scale is comparable to the component dimension, size effects are crucial for the evaluation of the part behavior. In metamaterials, size effects become especially pronounced when the corresponding structures are loaded in shear or bending [46]. As an example, when lattice beams are considered, the relative bending rigidity increases significantly when the size of the representative cell of the lattice approaches the thickness of the beam structure. This occurs if the beam structure is composed of very few layers of lattice cells in the thickness direction [16,17]. In such scenarios, the strain gradient extensions of the classical continuum models have received significant attention, not only for beam and plate structures [38,16,17] but also for three-dimensional solids [39–41]. They are proven to be accurate in predicting the mechanical behavior of size-dependent lattice structures. These beam theories are especially relevant when additively manufactured lattices are analyzed as the produced scales are rather small. However, as they require the effective Young's and shear moduli as input parameters, to the knowledge of the authors of this paper they have not been validated for the as-manufactured octet-truss lattices.

With this in mind, we aim to demonstrate and experimentally validate the proposed CT-based numerical framework which allows us to accurately evaluate the bending behavior of as-manufactured octet-truss lattice structures. To this end, the framework provides an efficient tool to compare the as-designed to as-manufactured properties under loading. Additionally, we investigate and validate the accuracy of the classical and the strain gradient beam theories by comparing their bending properties to the direct 3D numerical analysis of the as-manufactured and as-designed octet-truss lattice beams.

2. The Finite Cell Method for numerical analysis of CT scans

The as-manufactured shapes considered in this article are acquired via computed tomography. Such geometrical models challenge the meshing procedure of the conventional FEM approach. In particular, to prepare these structures for numerical analysis, a suiTable 3D model must be reconstructed. Then, a boundary conforming mesh must be generated. However, these two steps involve a lot of manual labor and necessary computational power. When the lattice structures are analyzed, the high level of microstructural details occurring in the manufactured geometries renders the preparation for the numerical analysis highly costly. Thus, to overcome these challenges, we introduce the Finite Cell method, an immersed boundary method. This approach allows for circumventing the challenge of preparing the CT-based geometrical models for numerical analysis by simplifying the mesh generation procedure and providing a natural way to incorporate these geometries into the numerical analysis directly. The main idea beneath the Finite Cell Method is illustrated in Fig. 1.

First, an arbitrary complex shape defined on a physical domain Ω is immersed in a simplified box-like domain Ω_e. Due to its simplicity, Ω_e can be trivially discretized with a structured grid of cuboids, further referred to as *finite cells*. These elements provide the support for shape functions which are chosen to be integrated Legendre polynomials of order p.

Second, the original boundary value problem must be recovered on the actual, physical domain. To achieve such a result, an indicator function $\alpha(\boldsymbol{x})$ is introduced into the problem formulation. It is defined to be equal to one on all points of the physical domain Ω

(a) Physical domain Ω

(b) Extended domain Ω_e

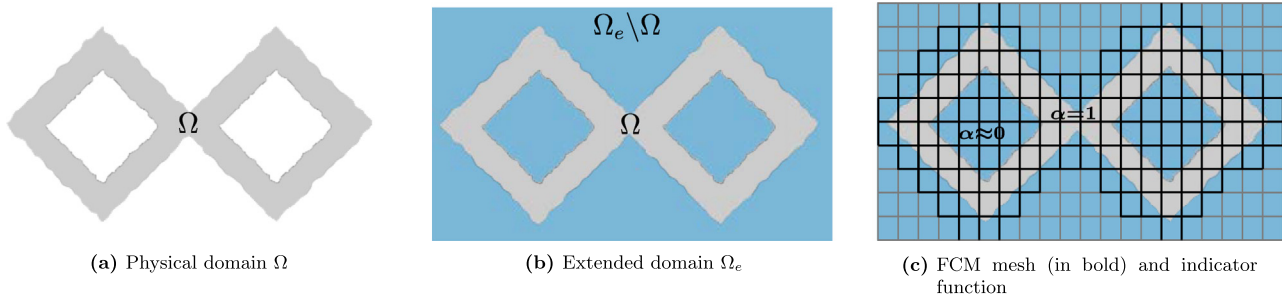(c) FCM mesh (in bold) and indicator function

Fig. 1. The idea of the Finite Cell Method.

and to a small positive value in the domain $\Omega_e \setminus \Omega$. Then, the modified linear elastic weak form of the problem can be written as follows:

Find $u_i(x_j) \in H^1_{\hat{u}}(\Omega_e)$ satisfying

$$\int_{\Omega_e} \alpha(x_i) C_{ijkl} \frac{\partial u_k}{\partial x_l} \frac{\partial \delta v_i}{\partial x_j} \, d\Omega_e + \beta_D \int_{\Gamma_D} u_i \delta v_i \, d\Gamma_D =$$
$$= \int_{\Omega_e} \alpha(x_i) b_i \delta v_i d\Omega_e + \int_{\Gamma_N} \hat{t}_i \delta v_i \, d\Gamma_N + \beta_D \int_{\Gamma_D} \hat{u}_i \delta v_i \, d\Gamma_D$$

(1)

with $H^1_{\hat{u}}(\Omega_e)$ being the first-order Sobolev space, $\hat{u}$ indicating a prescribed displacement on the domain boundary Γ_D, and $\hat{t}$ is prescribed traction on boundary Γ_N. In the present work, Dirichlet boundary conditions are enforced using the penalty method with the penalty parameter β_D.

As the geometries under consideration stem from CT images, the spatial scalar function $\alpha(\mathbf{x})$ can be conveniently related to the acquired Hounsfield scale. Since the analyzed parts are metallic lattices, the contrast between material and void in the scan is commonly very high.

Therefore, the threshold value of Hounsfield units HU_{thres} used to identify the metal and void regions in the CT scan images can directly be used to define the indicator function as follows:

$$\alpha(\mathbf{x}) = \begin{cases} 1 & \text{if } HU \geqslant HU_{thres} \\ \varepsilon, \varepsilon \ll 1 & \text{if } HU < HU_{thres} \end{cases}$$

(2)

Finally, as the indicator function makes the domain integrands in Eq. (1) discontinuous over the boundaries of the physical domain, a special integration rule should be applied. For this purpose, multiple techniques have been proposed (see, e.g., [1,20]). However, the most efficient integration rule for CT-based geometrical models is a voxel-based pre-integration introduced in [45]. In this case, the shape of an object is fully described by a grid of voxels with a constant Hounsfield scale. Such an underlying structure allows to further decompose every finite cell into a number of voxels $m_x \times m_y \times m_z$. Then, the standard $(p + 1)^3$ quadrature rule can be applied to every voxel resulting in $m_x(p + 1) \times m_y(p + 1) \times m_z(p + 1)$ integration points for one finite cell. Using these integration points, the integrands in Eq. (1) can be efficiently pre-computed for every voxel in an offline phase. Then, the resulting matrices are scaled in an online stage with the indicator function $\alpha(\mathbf{x})$ as in Eq. (2). Thus, this integration method provides an accurate and efficient technique to accurately compute the discontinuous integrands for CT-based geometries.

Although the Finite Cell Method in combination with a voxel-based pre-integration technique provides a powerful tool to perform numerical analysis directly on CT images, the size of the computed systems remains large. Large linear systems occur because as-manufactured structures include a considerable number of small-scale features, which are significant for the overall behavior of the parts. As an example, the largest CT scan considered further

in this paper has a resolution of $2096 \times 272 \times 128$ voxels, while the smallest significant geometrical variations have a size of $3 - 7$ voxels. To capture this behavior a relatively fine FCM mesh must be employed, thus, leading to a large number of degrees of freedom. An appropriate way to handle these large scale computational systems is to use a hybrid parallelization technique as the one introduced by Jomo et al. in [14,15].

3. Classical and strain gradient beam theories for uniaxial bending

Although one can expect that 3D numerical simulations on the as-manufactured AM lattices provide an accurate and realistic solution of the complex mechanical behavior, often a fast prediction is important for an early analysis stage. One of the approaches to obtain a quick solution is to use beam theories.

When slender beams with a small thickness-to-length ratio are considered, an Euler-Bernoulli model can be used to evaluate bending rigidity, while the Timoshenko beam theory is more appropriate when shear effects are not negligible. Both Euler-Bernoulli and Timoshenko beam models rely on the determination of the effective Young's modulus E^*, the moment of inertia I, and the effective shear modulus G^* for the latter model. These three quantities are not straightforward to obtain when lattice structures are considered. The two most common ways to determine them are to perform experiments or to use a first-order numerical homogenization. The octet-truss lattice forms an effectively three-dimensional orthotropic metamaterial from the material parameters of which one could obtain the effective material parameters (E^* and G^*) for beam models. Experimental measurements will be considered in this paper for the determination of the as-manufactured effective Young's modulus via a tensile test, while the numerical homogenization is used for the determination of as-designed effective quantities and as-manufactured effective shear modulus G^*. For a detailed description of the first-order CT-based homogenization employed in this article, interested readers are referred to [19]. However, when the size effects in the material characterization of lattice structures under bending play an important role in the macroscopic response, the classical beam theories might deliver incorrect results and must be further enhanced, e.g., by means of high-order models such as the strain gradient beam theory described in the following.

3.1. Three-point bending problem of lattice beams

In the present work, three-point bending of the AM lattice beams is investigated. The structure deforms in the xz-plane (see the 2D sketch of the problem in Fig. 2).

When utilizing the symmetry of the test set up in the axial direction and, accordingly, modelling the left half of the structure
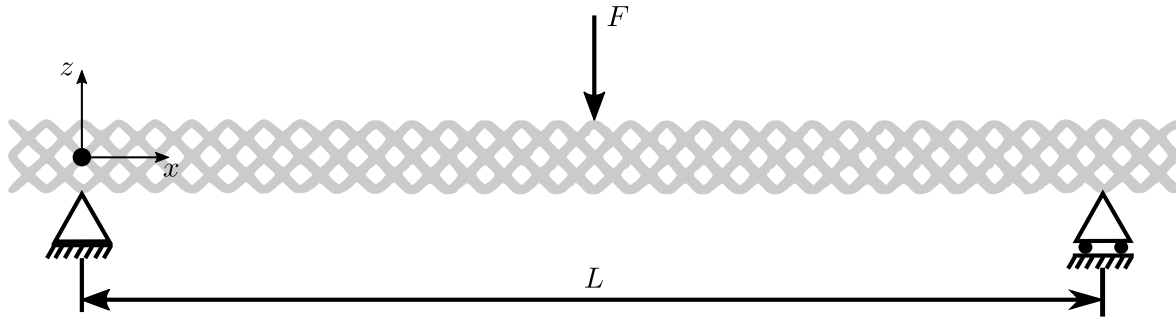
Fig. 2. A 2D sketch of a three-point bending setup.

as a uniaxial beam bending problem, the boundary conditions of the resulting beam problem read as follows:

$$w(x=0)=0, \qquad M(x=0)=0,$$
$$w'\left(x=\frac{L}{2}\right)=0, \quad Q\left(x=\frac{L}{2}\right)=\frac{F}{2} \tag{3}$$

where the x-coordinate runs along the central (neutral) axis of the beam and $x=0$ is the coordinate of a fixed left support, w is the deflection of a central axis of the beam, F is the applied force at the symmetry point $x=L/2$, whereas M and Q, respectively, are the standard bending moment and shear force of the beam.

3.2. Classical beam theories

Given the previously defined bending problem, the classical Euler-Bernoulli solution delivers the maximum deflection at $x=L/2$:

$$w^{EB} = \frac{FL^3}{48E^*I} \tag{4}$$

where L is the length of the beam, E^* is the effective Young's modulus. In the present work, we perform the homogenization such that the beam becomes a solid block made of homogeneous material with E^*. Hence, $I = (bh^3)/12$ is defined as an effective moment of inertia of a rectangluar cross section having the outer dimensions of the original structure.

To account for shear deformations for higher thickness-to-length ratios, the solution of classical Timoshenko beam theory for three-point bending can be formulated as follows:

$$w^T = \frac{FL^3}{4E^*I} + \frac{FL}{4G^*A} \tag{5}$$

where G^* is the effective shear modulus and A is the cross-sectional effective area. Then, the main characteristic of the bending behavior is the bending stiffness or bending rigidity. It defines the resistance of the specimens to bending deformations and is determined as follows:

$$D = \frac{F}{w} \tag{6}$$

where F is the applied load and w the determined displacement. With the help of the classical beam theories solutions, this quantity can be determined analytically when all other parameters are known. The classical Euler-Bernoulli bending rigidity for the considered problem can be written as follows:

$$D^{EB} = \frac{F}{w^{EB}} = \frac{48E^*I}{L^3} = \frac{4E^*bh^3}{L^3} \tag{7}$$

where b is the depth and h is the thickness of the homogenized rectangular cross section.

Analogously, the classical bending rigidity using the Timoshenko beam theory is defined as:

$$D^T = \frac{F}{w^T} = \frac{D^{EB}}{1+\frac{12E^*I}{G^*AL^2}} = \frac{D^{EB}}{1+\frac{E^*}{G^*}\left(\frac{h}{L}\right)^2} \tag{8}$$

Eq. (8) shows that for a fixed length L the bending rigidity D^T approaches D^{EB} when thickness approaches zero, whereas for constant thickness-to-length ratios the Timoshenko and Euler-Bernoulli rigidities stay apart.

3.3. Strain gradient beam theory

In the scope of the present work, we also consider strain gradient beam theories elaborated in [16,27].

In the following, the derivation for the Euler-Bernoulli beam is described in greater detail. The strain energy density for a 3D body following Mindlin's strain gradient elasticity theory of form II is formulated as follows [26]:

$$\mathscr{W}_{II} = \frac{1}{2}C_{ijkl}\varepsilon_{ij}\varepsilon_{kl} + \frac{1}{2}A_{mijnkl}\partial_m\varepsilon_{ij}\partial_n\varepsilon_{kl} \tag{9}$$

where C_{ijkl} and A_{mijnkl} stand for the linear and high-order elasticity tensors, ε_{ij} is the engineering strain tensor, and $\partial_m\varepsilon_{ij}$ and $\partial_n\varepsilon_{kl}$ denote the partial strain gradient.

Then, the dimensional reduction to the strain gradient Euler-Bernoulli beam theory is performed. The displacement components $\boldsymbol{u} = (u_x, u_y, u_z)$ obey the same relationships as for the classical beam theory:

$$u_x = -z\frac{\partial w(x)}{\partial x}, \qquad u_y = 0, \qquad u_z = w(x) \tag{10}$$

where x is the coordinate along the main axis of the beam, z is the direction perpendicular to it, and y is the out-of-plane coordinate, as depicted in Fig. 2. This leaves the transverse deflection w as the only unknown. The stretching and bending states are decoupled since small deflections allow geometrically linear analysis. Furthermore, the octet-truss lattice forms a three-dimensional orthotropic metamaterial. Thus, when the beam structures are formed by aligning the central axis along one of the material directions, the material symmetry with respect to this axis is preserved (see, e.g., Fig. 2 and later explanation in Section 4).

Furthermore, the only non-zeros strain and stress components are ε_{xx} and $\sigma_{xx} = C_x\varepsilon_{xx}$ with $C_x = C_{xxxx}$. Accordingly, the model incorporates strain gradients $\varepsilon_{xx,x}$ and $\varepsilon_{xx,z}$ only, with the corresponding two high-order elasticity constants $A_x = A_{xxxxxx}$ and $A_z = A_{xxzxxz}$ [36]. Then, the variation of the strain energy corresponding to Eq. (9) simplifies to:

$$\delta \int_\Omega \mathscr{W}_{II}d\Omega = \int_\Omega (C_x\varepsilon_{xx}\delta\varepsilon_{xx} + A_x\varepsilon_{xx,x}\delta\varepsilon_{xx,x} + A_z\varepsilon_{xx,z}\delta\varepsilon_{xx,z})d\Omega \tag{11}$$

and further to a 1D energy expression over the main axis of the beam:

$$\delta \int_\Omega \mathscr{W}_{II} d\Omega = \int_0^L \left(M + g_z^2 R\right) \frac{\partial^2 (\delta w)}{\partial x^2} dx + \int_0^L g_x^2 \frac{\partial M}{\partial x} \frac{\partial^3 (\delta w)}{\partial x^3} \tag{12}$$

with a generalized moment $R(x)$ written out as follows:

$$R(x) = \int_A \frac{\partial \sigma_{xx}(x,y,z)}{\partial z} dA = C_x A \frac{d^2 w}{dx^2} \tag{13}$$

where $A = A(x)$ is the cross-sectional area of the beam.

Applying the Hamilton's principle the strong formulation of the two-parameter strain gradient Euler-Bernoulli elasticity model can be finally formulated. The differential equation reads in terms of moments, or in terms of deflection with constant material parameters, respectively, as follows:

$$(M + g_z^2 R - (g_x^2 M')')'' = f \quad \text{or} \quad (E^* I + g_x^2 E^* A) w'''' + g_x^2 E^* I w'''''' = f \quad \forall x \in (0, L) \tag{14}$$

where f is the externally applied transversal loading and $E^* I$ stands for the classical bending rigidity with $E^* = C_x$, whereas the two length scale parameters g_x and g_z are defined by relations $A_x = g_x^2 E^*$ and $A_z = g_z^2 E^*$, respectively. As the higher-order term $((g_x^2 M')')''$, (or $g_x^2 E^* I w''''''$) can be related to boundary layer effects specific for certain boundary conditions and the crucial stiffening effect can be traced back essentially to the additional lower-order term $g_z^2 R$, (or $g_z^2 E^* A w''''$) (see [27]), the governing equation can be written in a simple lower-order form [16,17]:

$$(E^* I + E^* A g^2) w'''' = f \qquad \forall x \in (0, L) \tag{15}$$

where only one length scale parameter $g = g_z$ is present.

The analytical solution of Eq. (15) under the absence of body load with the boundary conditions described in Eq. (3) takes the form:

$$w_{gr}^{EB} = \frac{F L^3}{48 \left(E^* I + E^* A g^2\right)} \tag{16}$$

Eq. (16) compared to the solution of the classical Euler-Bernoulli theory in Eq. (4) introduces the intrinsic length scale parameter g which acts as a high-order material parameter depending on the microstructure of the unit cell. This parameter characterizes the size-dependent beam behavior when the thinnest beams show a stiffening effect.

The solution of the strain gradient Timoshenko beam theory can be derived in a similar manner taking into account the respective assumptions [16,17]:

$$w_{gr}^{T} = \frac{F L^3}{48 \left(E^* I + E^* A g^2\right)} + \frac{F L}{4 G^* A} \tag{17}$$

Eq. (17) is also similar to the solution of the classical Timoshenko theory except for the presence of the intrinsic material parameter g. The bending rigidities (with rectangular cross sections $A = bh$) corresponding to these deflections can be shown to follow, respectively, the formulae:

$$\begin{aligned} D_{gr}^{EB} &= D^{EB} \left(1 + 12\left(\tfrac{g}{h}\right)^2\right) \\ D_{gr}^{T} &= D^{T} \left(1 + 12\left(\tfrac{g}{h}\right)^2\right) \end{aligned} \tag{18}$$

revealing the size effect for decreasing values of h with a fixed value of g.

To sum up, both the classical and the strain-gradient theories could provide a quick estimate of the bending behavior of the considered beam-like lattice structures. In the following, the predictions provided by these theories will be compared to the full 3D numerical and experimental analysis performed on the AM octet-truss beams. Furthermore, their accuracy and applicability will be evaluated with the help of experimental three-point bending tests.

4. Experimental setup

The experimental and numerical investigations are held on octet-truss lattices. A representative unit cell of such structures is depicted in Fig. 3. As the main focus of the present work is the investigation of lattice bending behavior, an octet-truss unit cell indicated in Fig. 3 is used to construct the four beam-like structures shown in Fig. 4. These beams have the same length of 128 mm (32 cells) and the same width of 8 mm (2 cells) but different heights (thicknesses): 4, 8, 12, and 16 mm, respectively (1, 2, 3, and 4 unit cells). Then, the upper and the lower side of the beams was completed to contain the full strut size of 0.8 mm (see zoomed side of a representative specimen in Fig. 5). These complements were added for the printing resolution and for the assumption that possible applications would most probably include such complements. According to CAD-based FE-simulations, trusses with and without these complements behave almost identically, both qualitatively and quantitatively. Therefore, the total heights of the specimens are 4.8, 8.8, 12.8, and 16.8 mm. Thus, the constructed thickness-to-length ratios are 0.03, 0.06, 0.09, and 0.13 respectively.

The specimens for experimental testing were printed in the laboratory 3DMetal@UniPV using a selective laser melting metal 3D printer Renishaw AM400. For the production of the specimens, stainless steel powder SS 316L-0407 was used. According to the material data sheet of the producer [33], the considered setup leads to a bulk material with Young's modulus 190 GPa $\pm$ 10GPa in the printing direction. This value as indicated in the data sheet depends on the printing direction. In the orthogonal direction to the printing the Young's modulus is reported to be
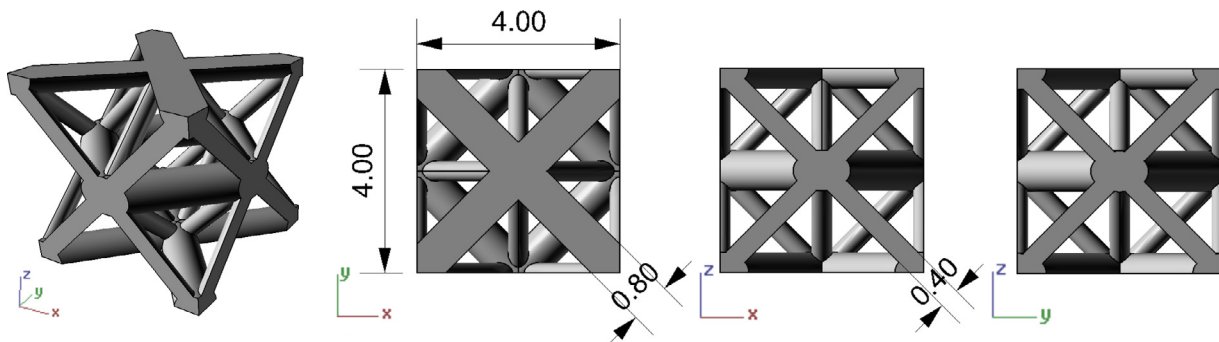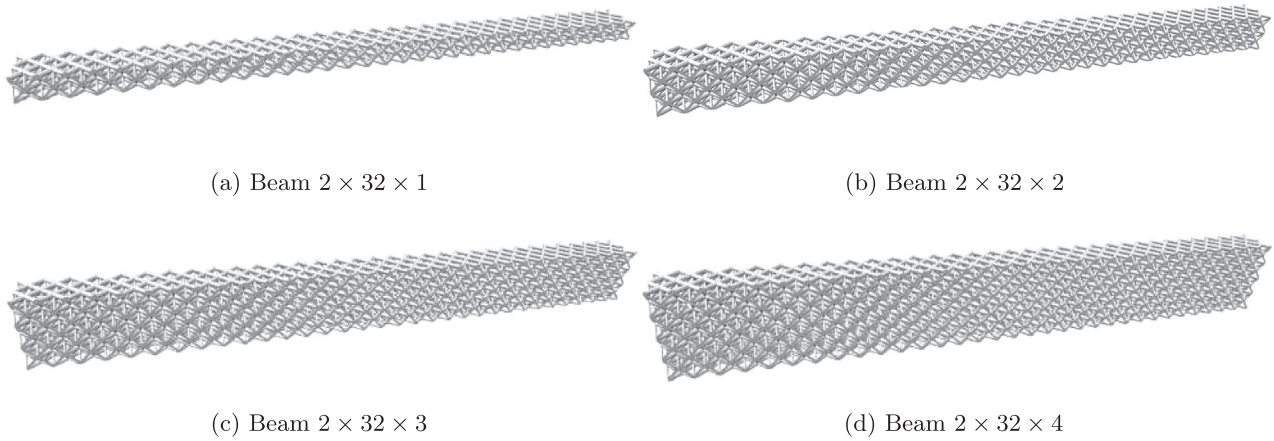

Fig. 3. CAD model of the octet-truss unit cell [18].

(a) Beam $2 \times 32 \times 1$

(b) Beam $2 \times 32 \times 2$

(c) Beam $2 \times 32 \times 3$

(d) Beam $2 \times 32 \times 4$

Fig. 4. Investigated CAD models of the octet-truss beam structures.
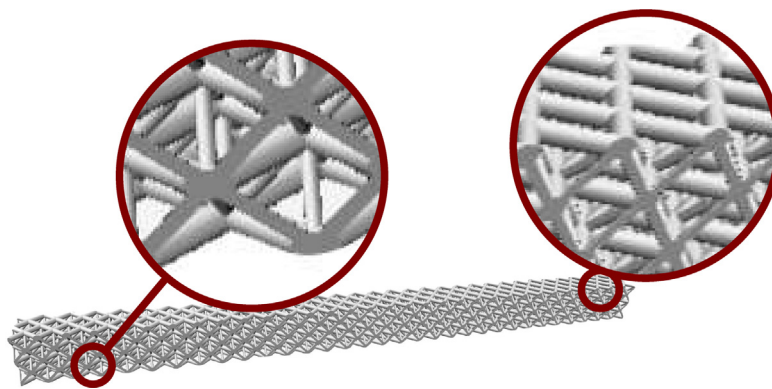

Fig. 5. Zoom on the completed upper and lower struts of the beam $2 \times 32 \times 2$.
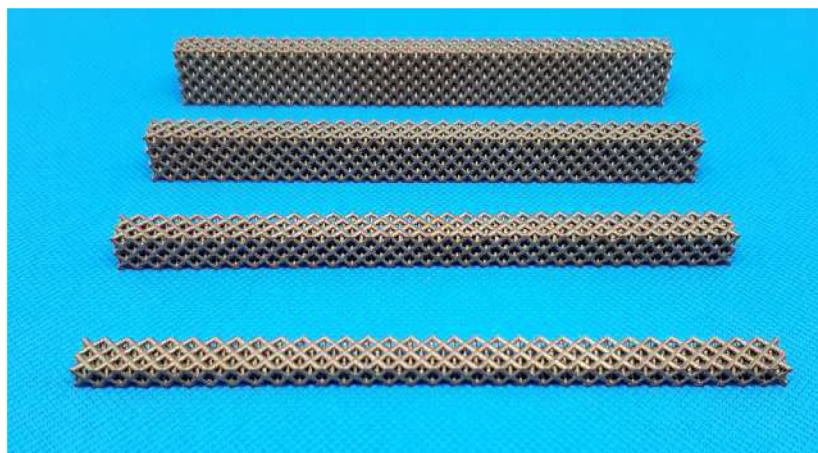

Fig. 6. Printed specimens after heat treatment.

Table 1
Dimension comparison of the beam specimens (D stands for as-designed, M stands for as-manufactured).

Specimen	Width [mm]		Height [mm]		Length [mm]	
	D	M	D	M	D	M
$2 \times 32 \times 1$	8.00	8.22 ± 0.001	4.80	4.96 ± 0.002	128.00	$128.82 \pm 1e-4$
$2 \times 32 \times 2$	8.00	8.22 ± 0.001	8.80	8.89 ± 0.002	128.00	$128.83 \pm 1e-4$
$2 \times 32 \times 3$	8.00	8.22 ± 0.001	12.80	12.89 ± 0.001	128.00	$128.91 \pm 1e-4$
$2 \times 32 \times 4$	8.00	8.22 ± 0.001	16.80	16.96 ± 0.001	128.00	$128.91 \pm 1e-4$

197 GPa $\pm$ 4 GPa. As these two values are fairly close to each other, in the following we will assume an isotropic material with the Young's modulus being 190 GPa. The produced specimens after heat treatment at 400°C in the chamber Nabertherm LH120/12 for 2 h are shown in Fig. 6.

Prior to performing any experimental test, the four bending specimens were subjected to a computed tomography to acquire the as-manufactured geometries. The CT scans were performed with a Phoenix V CT scanner with a resolution of 61 μm.

Then, to validate the numerical frameworks proposed in Section 2 and 3, four main quantities were determined experimentally. These are the as-manufactured dimensions, porosity of the printed lattices structures, the effective Young's modulus, and the bending rigidity.

As-manufactured samples dimensions

As the deviation of the as-manufactured and as-designed overall dimensions are expected, the corresponding measurements are performed experimentally. In particular, an overall width, height and the length of the printed beam specimens is measured with the help of a digital caliper. Table 1 summarizes the experimentally determined values together with the designed characteristics. As there is no repetitive measurement available, we provide the measurement uncertainty of the used instrumentation. The measurement uncertainty is computed according to [13] using the uncertainty propagation of the used instrument's precision. As the dimensions of the as-manufactured samples are measured with the digital calipers, the instrumentation error of this device is used to evaluate the measurement error. The results are indicated in Table 1.

The values shown in Table 1 are used in this article to compute the effective cross-sectional area A and the effective cross-sectional moment of inertia I of the as-designed and as-manufactured specimens. Both, A and I are determined by using the outer dimensions of the beams. Furthermore, these values are used to identify the as-manufactured porosity as described in the following paragraph.

Porosity of the printed structure

The overall porosity of the lattice structures is measured for two reasons. The first motivation is to compare the experimentally determined porosity value to the as-designed CAD-based ones, thus, providing the first estimate on the geometrical variations of the as-manufactured geometries with respect to the original CAD models shown in Fig. 4. The second reason is to experimentally verify the porosity values determined from the acquired CT scan of every beam. The porosity values are determined by evaluating the mass of the specimen m. Then, considering the printed density ρ indicated in [33] the overall porosity can be calculated as:

$$\phi = 1 - \frac{m}{\rho V} \tag{19}$$

where V is the measured volume of the bounding box of the specimen. The porosity is measured for a single sample of every setup indicated in Fig. 4. To compute the porosity according to Eq. (19), the high-precision scale is used to evaluate the mass of the specimen m. The volume of the overall bounding box of the specimen is computed using the measured values from Table 1. Thus, their instrumentation precision is considered and indicated as the measurement uncertainty in Table 2.

Table 2
Porosity comparison of the beam specimens.

Specimen	CAD-based porosity [–]	Experimental porosity [–]	CT-based porosity [–]
2 × 32 × 1	0.756	0.638 ± 0.006	0.647
2 × 32 × 2	0.770	0.630 ± 0.004	0.639
2 × 32 × 3	0.775	0.677 ± 0.003	0.679
2 × 32 × 4	0.777	0.630 ± 0.002	0.671

Fig. 7. Experimental setup of a tensile experiment on an octet-truss lattice structure [18].

Effective Young's modulus

The second quantity of interest is the effective Young's modulus of the octet-truss lattice. This value is important for the investigation of the applicability of the beam models as described in Section 3. The as-manufactured effective Young's modulus E^* is determined via a tensile test of the sample lattice specimens. The experiment is performed in the material mechanics laboratory with the help of the MTS Insight System. For the elongation measurements, a video extensometer is used (see experimental setup in Fig. 7). The effective Young's modulus is then computed according to ASTM E111 standard [2]. The determined value is $E^* = 12\,533 \pm 751$ MPa together with the corresponding measurement error.

Bending rigidity

The final experimentally determined value is the bending rigidity of the octet-truss lattice beams as defined in Eq. (6). This quantity describes the characteristic overall (global) resistance of the structure against the bending deformation. The values of bending rigidity of the four 3D printed structures of Fig. 6 is experimentally measured by a three-point bending test under quasi-static conditions and displacement-controlled velocity (see Fig. 8). The span (L) between the supports is 120 mm, while the applied point load (F) is transferred in the middle of the span of the beam. During the experiment, the imposed displacement and the corresponding force are recorded. The bending rigidities of the beams are then computed by using Eq. (6). Similar to the evaluation of porosity, we indicate the measurement uncertainty stemming from the used instrumentation. In particular, the precision of the video extensometer, the force measurement precision, and the uncertainty of the initial length measurement using the digital calipers is considered. All tests are performed in both elastic and plastic regime. However, for the aim of this work only the elastic characteristics are considered. Experimental results will be discussed together with the numerical values in the following sections.

5. Numerical investigations

In this section, the results of the numerical investigations on the octet-truss lattices are discussed in detail.

First, the behavior of the octet-truss lattice structures undergoing a bending load case is analyzed numerically in Section 5.1. In this section, the as-manufactured and as-designed octet-truss beams are compared geometrically and the differences are quantified by means of the macroscopic porosity defined in Eq. (19). Then, the direct numerical simulation of the three-point bending
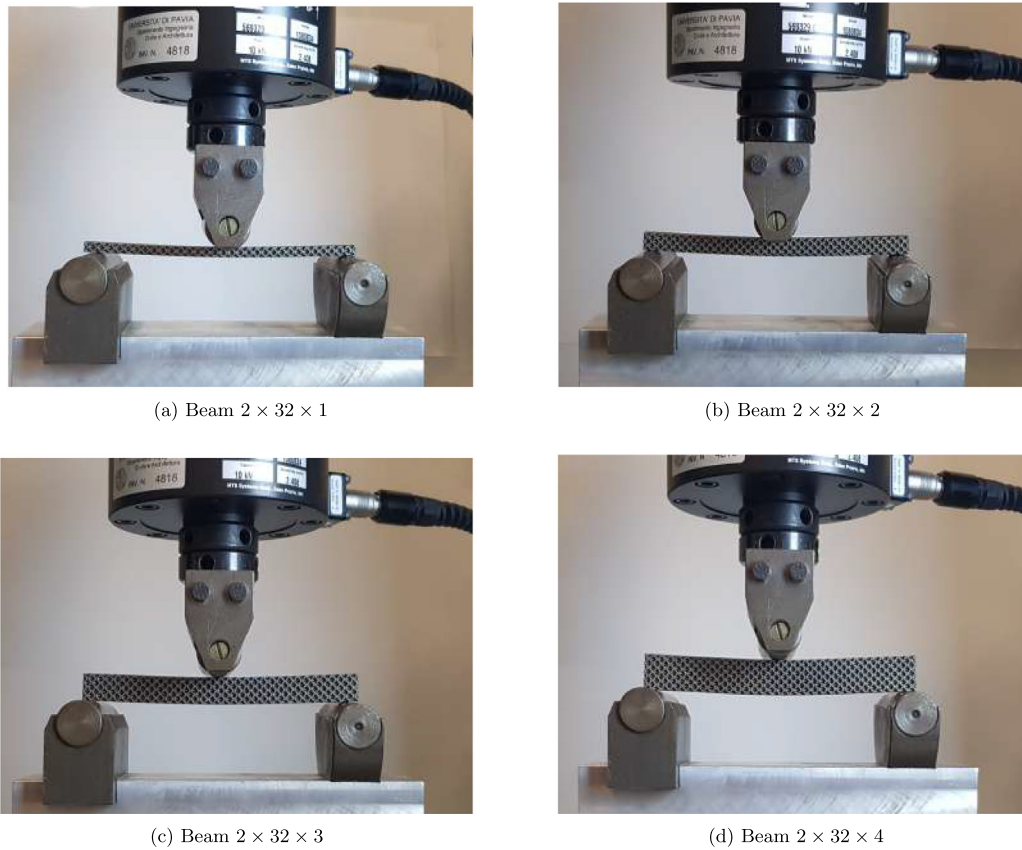
(a) Beam $2 \times 32 \times 1$

(b) Beam $2 \times 32 \times 2$

(c) Beam $2 \times 32 \times 3$

(d) Beam $2 \times 32 \times 4$

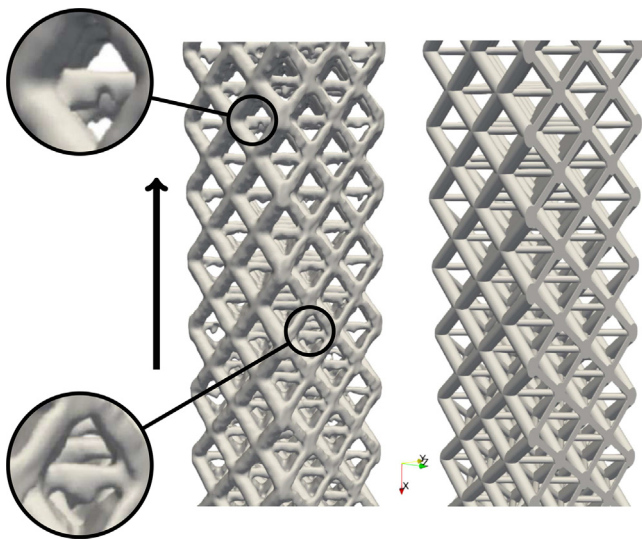**Fig. 8.** Bending of beam specimens.

Fig. 9. Zoom on the geometrical features of the as-manufactured (left) and as-designed (right) bending specimen (build direction marked with the black arrow).

Fig. 10. Comparison of as-manufactured and as-built octet-truss bending specimen $2 \times 32 \times 2$ (build direction marked with the black arrow).

test is performed on both CAD and CT geometries. The properties of the bulk material are assumed to be isotropic with the values indicated in Section 4. All numerical investigations with the Finite Cell Method are performed using the extensively verified and validated in-house immersed high-order FEM code *AdhoC++* continuously developed at the Chair of Computational Modeling and Simulation of TUM (see, e.g., [7,9,10,44]). The achieved numerical results are finally compared to the experimental values.
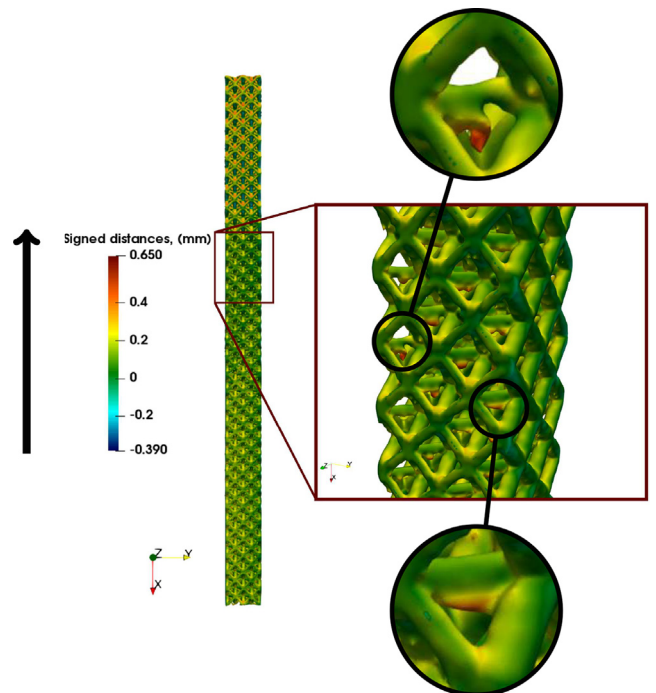
Second, in Section 5.2, the applicability of the beam theories described in Section 3 is investigated. Both, the classical and the

strain-gradient Euler-Bernoulli and Timoshenko beam theories are applied to analyze the behavior of both as-designed and as-manufactured octet-truss lattice beams.

5.1. Comparison of as-manufactured and as-designed mechanical behavior in bending

Geometrical comparison

To highlight the macroscopic differences between the as-manufactured geometry extracted from CT scan images and the as-designed geometric model, zoomed views on both geometries are depicted in Fig. 9. From a thorough comparison of the two geometric models (see Fig. 10), the following geometrical features of as-manufactured geometry can be observed compared to the as-designed ones:

- larger truss thickness;
- partially melted material powder particles in overhanging surfaces opposite to the build direction;
- excess material collection in the nodes.

These features are well-known side effects of the SLM printing process. It is also established in literature [3,6,18], that these geometrical features have a strong influence also on the numerical results, and thus as-designed models lead to a quite inaccurate prediction of the mechanical behavior of lattice structures.

To obtain the depicted CT geometries, the threshold value of Hounsfield units HU_{thres} has to be determined. As indicated in Eq. (2), this value is also essential to perform the Finite Cell analysis on the as-manufactured geometries. This process of image segmentation is well-established in the field of medical imaging. Although this work's application area is metal CTs, we employ the same algorithms to segment the CT images of the octet-truss structures. In the following, the single threshold technique is used to identify the threshold value (see, e.g., [28] and the literature cited therein). In particular, as the beams' material is metal and the size of the features is relatively large for the μCT scan, the contrast in the obtained images is very high. Thus, the image has a bimodal histogram of the intensity values. To simplify the determination technique, we employ Otsu's global thresholding technique [28]. This provides a good estimate of the necessary value relying on the fact that the CT image histogram is bimodal. Of course, there is a particular transition area which justifies a slightly varying HU_{thres}. However, the determined values were used in this work

"as is" without further modifying its values. To quantify the obtained results, as described in Section 4 the CT-based porosity values are compared to the CAD-based and experimental ones. Table 2 summarizes the achieved results. As expected, the CAD-based porosity is always larger than the printed one. This is also supported by the geometrical comparison of the CAD and CT-based model (an example of specimen $2 \times 32 \times 2$ is shown in Fig. 10). The excess material collection in the nodes together with the larger truss thickness leads to a lower manufactured porosity. Overall, the CT-based porosity is in good agreement with the experimental values, making us confident in the sufficient accuracy of the as-manufactured geometry representation provided by CT scan measurements. However, the porosity value of the thickest beam differs from the experimentally determined value by 6.5%. Although there is a certain possibility to vary the threshold value of the CT scan, the experimental porosity value cannot be achieved within a reasonable range of variation of HU_{thres}. Curiously, the beam with $2 \times 3 \times 32$ cells indicates an increase in the experimental porosity, which is also observed in the CT scan. This tendency, however, seems to be reversed in the case of the thickest beam.

Direct numerical simulations of three-point bending test

In order to further support the above observations, we carry out a numerical simulation of the three-point bending test described in Section 4. Numerical experiments are performed for each one of the four specimens on both as-designed (CAD) and as-manufactured (CT) geometrical models. In both cases, the same boundary conditions and load cases are applied as in the experimental setup. The simulation of the as-designed geometry is carried out by using Comsol™, with quadratic tetrahedral Finite Elements, whereas as-manufactured geometry is simulated using the Finite Cell Method as described in Section 2. The latter is performed directly on the complete CT image. A complete scan of every beam specimen is immersed in a grid of finite cells of polynomial degree $p = 3$ containing $2 \times 2 \times 2$ voxels. An example of the used discretization for the analysis of the beam specimen depicted in Fig. 10 is depicted in Fig. 11. Fig. 11 shows a complete finite cell mesh with two consequent zooms on the corner of this model. As an example, for this specimen a total number of $51 \times 524 \times 32$ cells is used. The authors would like to emphasize, that no simplifications are carried out to incorporate the as-manufactured geometry in the direct numerical analysis.

Representative displacement and von Mises stress distributions for an as-manufactured beam specimen are shown in Fig. 12.
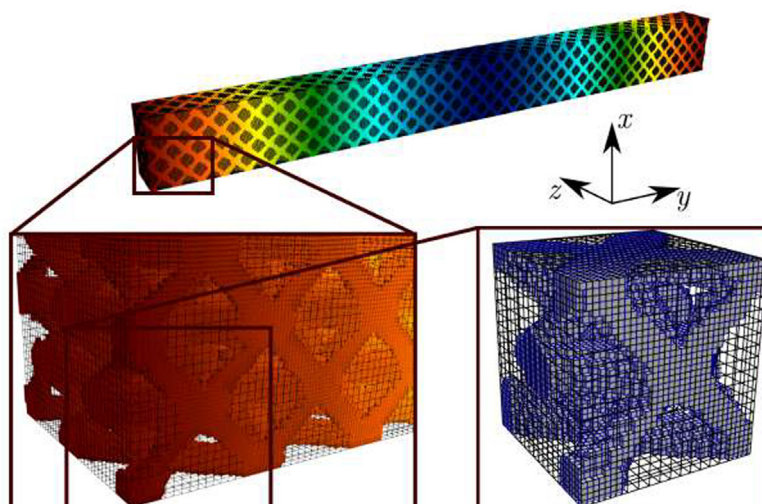

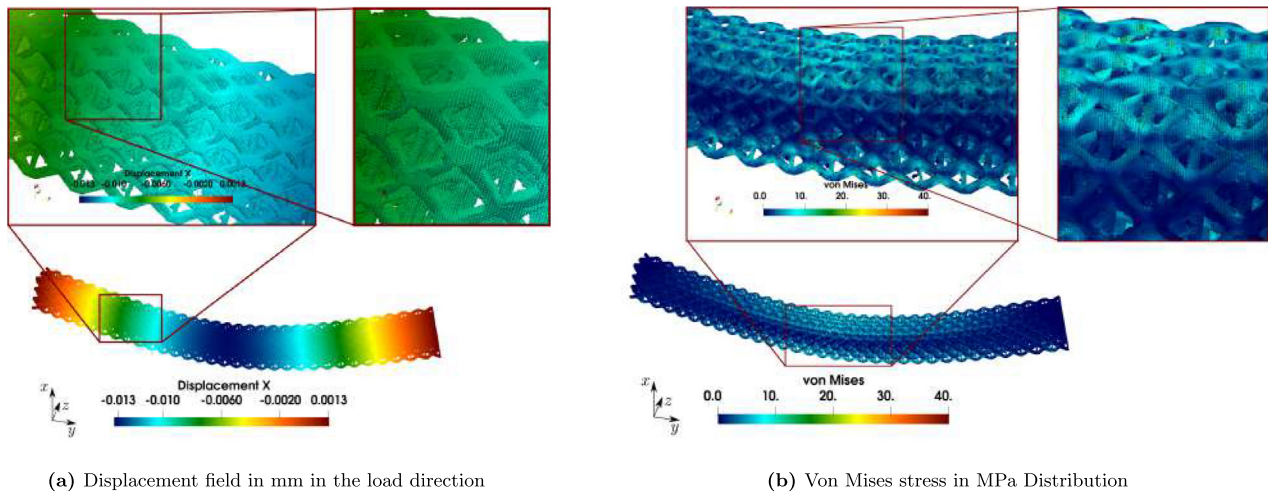**Fig. 11.** Finite Cell mesh with $51 \times 524 \times 32$ cells for $2 \times 3 \times 32$ beam specimen.

(a) Displacement field in mm in the load direction

(b) Von Mises stress in MPa Distribution

Fig. 12. Displacement and von Mises stress distributions for as-printed beam $2 \times 3 \times 32$ utilizing the Finite Cell Method.
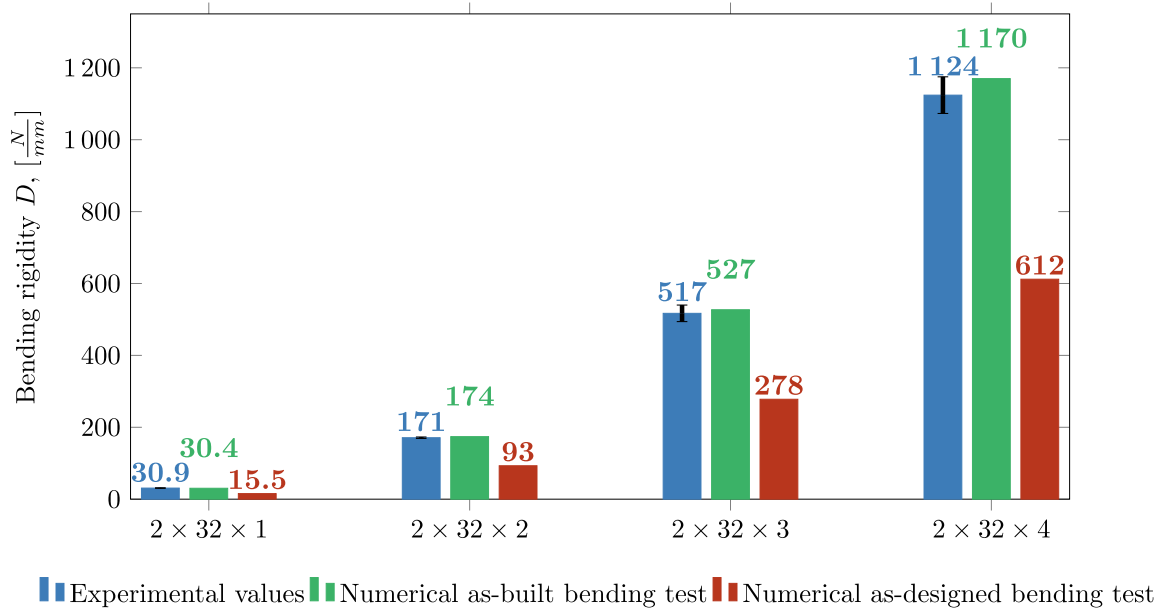

Fig. 13. Comparison of bending rigidity obtained by numerical bending tests on the original as-designed geometry and on the as-manufactured geometry obtained from CT-scan data.

The numerical bending rigidities are, then, computed by using Eq. (6) and their values are compared to the experimental ones in Fig. 13. To provide an insight into the necessary computational resources, the simulation of the as-designed beam of $2 \times 3 \times 32$ is performed on the standard workstation with i7-9700 K processor and 64 GB of RAM using shared memory parallelism. The total wall clock time for the computation amounts to 2 min including pre- and postprocessing. By contrast, the simulation of the as-manufactured geometry on the cluster using the distributed memory parallelism on 40 28-way Haswell-based nodes with 64 GB RAM takes 37 min. This large difference is due to the fact that the latter model incorporates many more small scale details.

The qualitative comparison of these results shows that the as-designed and as-manufactured geometries follow the same tendency of a higher rigidity value for thicker beams. Nevertheless, quantitatively the relative errors in the bending rigidity value are always above 40%. This gap is largely driven by the geometrical difference between the as-manufactured and as-designed geome-

tries. As the CT-based and experimental porosity values shown in Table 2 are lower than the designed ones, the as-designed bending rigidity should agree with this trend. According to the results in Fig. 13 the as-manufactured bending rigidity is larger than the designed one, thus, supporting the described tendency. Furthermore, the numerical simulation on the printed geometry via computed tomography provides an excellent agreement with the experimental tests, with a relative error always below 4%. Interestingly, although the porosity determined by a CT scan for the thickest beam is lower than the porosity determined experimentally

Table 3

Effective mechanical quantities of the octet-truss specimens.

Effective quantity	As-designed	As-manufactured
E^*, MPa	7356	$12,533 \pm 751$[a]
G^*, MPa	2742	5651

[a] Experimental measure.

(see Table 2), the numerical bending rigidity for this specimen is slightly higher than the experimental value. The dependency between the porosity and the bending rigidity of the samples is, in general, non-linear. This is similar to the tensile characteristics, such as the homogenized Young's modulus (see [18]). However, the results are "reversed" in this case. As the experimental value is obtained by measuring one specimen, this could suggest that the CT-based porosity provides a more accurate estimate. Furthermore, this would support the trend of a slightly higher porosity value for thicker beam setups as described in the previous section.

5.2. Experimental validation of strain gradient beam theory for octet-truss lattices

Since in a three-point bending it is often desired to predict the mechanical behavior by dimensionally reduced beam models, we investigate more carefully the applicability of the beam models described in Section 3 to octet-truss lattice structures.

The beam models rely on the identification of effective quantities, such as Young's modulus E^* and shear modulus G^*. As briefly mentioned in Section 3, there are two ways to obtain the necessary quantities. For the as-designed geometries, only the first-order mean-field homogenization can be applied, as there is no possibility to perform experimental tests on it, while for the as-manufactured structures, the effective Young's and shear modulus can be measured experimentally. In the scope of this work, only the as-manufactured Young's modulus of octet-truss lattices is experimentally evaluated, whereas the effective as-manufactured shear modulus is determined by means of the first-order mean-field homogenization technique mentioned in Section 3. To account for non-periodic as-manufactured cells, the homogenization is performed through the whole structure, taking the mean value of the homogenized shear modulus similar to the identification procedure of the homogenized Young's modulus described in [18]. Table 3 summarizes the effective quantities used in the following.

Furthermore, to apply the beam theories described in Section 3 the effective cross-sectional area A and the moment of inertia I have to be computed. These quantities are dependent on the overall dimensions of the beam specimens. The as-designed and as-manufactured values as indicated in Table 1 are different. Thus, the values indicated with D in Table 1 are used to compute the effective geometrical characteristics of as-designed models, while the ones indicated with M in Table 1 of as-manufactured shapes.

Fig. 14 shows the normalized bending rigidity D/D^{EB} with respect to the beam height h (see Eq. (7)). The normalization is performed with respect to the Euler-Bernoulli bending rigidity D^{EB} solution as follows:

$$\frac{D}{D^{EB}} = \frac{Dw^{EB}}{F} = \frac{w^{EB}}{w} \tag{20}$$

where w^{EB} is the classical Euler-Bernoulli solution for three-point bending as in Eq. (4), w is the experimentally recorded maximum deflection, and D is the compared bending rigidity.

As the as-manufactured and as-designed geometries have different geometric and mechanical effective properties, the bending rigidities are normalized with the Euler-Bernoulli solutions using the respective quantities from Table 3 and, thus, they are plotted separately in Fig. 14a and b.

In both plots of Fig. 14, the dashed lines indicate the results predicted by the classical beam theories, while the solid lines stand - the strain-gradient beam theories. The blue dots correspond to the experimental bending rigidity, whereas the crosses indicate the results of the numerical bending simulation computed on the as-manufactured specimen from Fig. 13. Both values are normalized

with the analytical Euler-Bernoulli solution using the as-manufactured effective Young's modulus from Table 3. The brown dots in Fig. 14b indicate the CAD-based results of the numerical bending test and again the results are normalized with the Euler-Bernoulli solution with the as-designed effective Young's modulus from Table 3. Since as-designed geometry allows for further reduction of the considered thickness-to-length ratios, an extra point is added at the height of 2.4 mm. This setup leads to a thickness-to-length ratio of 0.015.

Classical beam theory using as-manufactured and as-designed geometry

As the normalization is performed with respect to the corresponding classical Euler-Bernoulli solution, the dashed black lines remain at the value 1 for both as-manufactured and as-designed geometries. If the octet-truss lattice beams were to follow this behavior, all bending rigidities would lay on a straight line. However, neither as-manufactured nor as-designed values seem to comply with the assumptions of the Euler-Bernoulli theory. Thus, the classical Euler-Bernoulli theory cannot be applied to the characterization of the bending behavior of the considered octet-truss lattices.

The classical Timoshenko beam theory indicated with the green dashed line converges to the Euler-Bernoulli theory with the decreasing beam height. These states correspond to extremely slender beams, thus, making shear effects of minor importance. The as-manufactured geometry results as shown in Fig. 14a propose that only the thickest specimen with $2 \times 32 \times 4$ cells and the thickness-to-length ratio of 0.13 follows the Timoshenko theory. However, the rest of the points do not follow this curve. The as-designed bending behavior as depicted in Fig. 14b shows a similar trend, where for the thickest specimens the points lay on the curve. Although the Timoshenko beam theory seems to provide a better solution compared to Euler-Bernoulli, none of them can capture the observed bending behavior well.

Strain gradient beam theory using as-manufactured geometry

Fig. 14a indicates the presence of a stiffening effect. When the height of the beam is close to the characteristic size of the unit cell, the size effects affect the macroscopic bending behavior of the components and cause stiffer behavior in comparison to a standard prediction of the classical beam theories. This size-dependent bending phenomenon is precisely captured by the strain gradient beam theories on the as-manufactured geometries.

The strain gradient beam theories as described in Section 3 introduce an additional material parameter g. This high-order parameter is unknown a priori and can only be determined by a calibration of the solid lines to the obtained numerical and experimental solutions (or by other generalized homogenization procedures [12]). As mentioned in [16], this intrinsic length parameter behaves as a material parameter and it is independent of loading, problem type, or the beam model. This quantity only depends on the underlying geometry. Thus, it must be the same for both strain gradient Timoshenko and Euler-Bernoulli theories. The value of the high-order material parameter g is determined as 0.349 [mm] for the as-manufactured octet-truss lattice (see Table 4). This intrinsic length parameter characterizes the size effects in the octet-truss lattice structures via both Euler-Bernoulli and Timoshenko strain gradient beam theories. Its order is close to the smallest strut size diameter of the unit cell of 0.4 [mm].

Although both strain gradient beam theories seem to capture an overall stiffening trend, it is important to know which theory is applicable. The numerical solution indicated with crosses seems to rather follow the Euler-Bernoulli approximation. However, the experimental data indicated with blue dots do not give a clear direction of which theory to follow. The first three points lay on the strain gradient Euler-Bernoulli theory, while the last point cor-
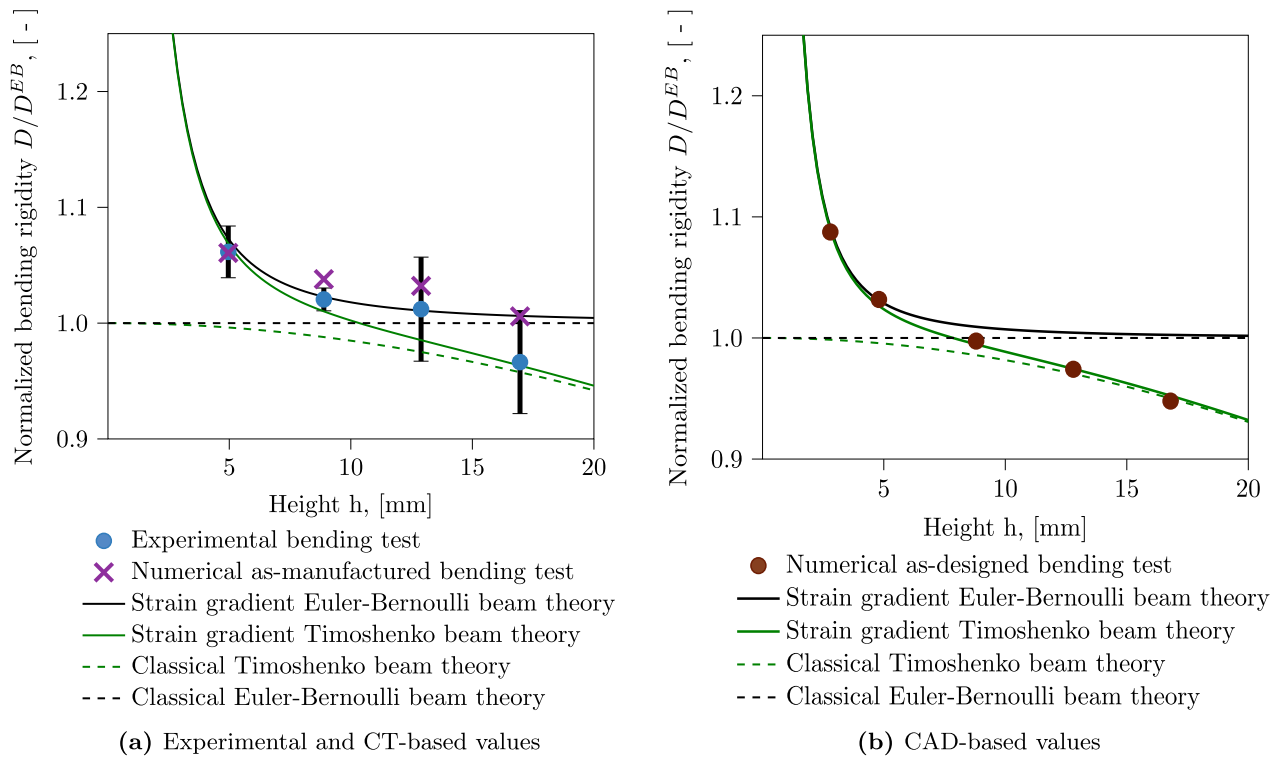
(a) Experimental and CT-based values

(b) CAD-based values

Fig. 14. Normalized bending rigidities of the octet-truss lattice beams with respect to the beam height.

Table 4
Comparison of as-designed and as-manufactured high-order intrinsic length parameter of the octet-truss specimen.

	As-designed g [mm]	As-manufactured g [mm]
Octet-truss beam	0.244	0.349

responding to the thickness-to-length ratio 0.13 seems to be away from it. This can suggest that for the last configuration the strain-gradient Timoshenko theory is more appropriate. However, the measurement error bars on the experimental data indicate that both theories could be applicable for this setup and the last point can as well lay on the black solid line. Furthermore, the CT-based porosity value for the thickest beam is further away from the experimental one. Thus, it could lead to uncertainty in the computed bending rigidity. To further clarify this let us look at the as-designed results.

Strain gradient beam theory using as-designed geometry

As already pointed out, the effective quantities obtained on the as-designed model are far from the experimentally determined bending rigidity and are depicted separately in Fig. 14b.

Curiously, for the as-designed geometry, a weaker stiffening effect is observed. For the thickness-to-length ratio of 0.03 (i.e., for the thinnest beam), the CAD-based results show about 8.4% stiffening compared to the thickest observation, while the as-printed analysis indicated 9.5%.

This is also reflected in the intrinsic high-order material parameter g. It is determined as $g = 0.244$ mm in the same manner as for the as-manufactured geometries (see Table 4). The most remarkable observation is that this high-order material parameter is lower than the one for as-manufactured geometries, similarly to the behavior already observed in the porosity values, the effective quantities, and the bending rigidity of the octet-truss specimens.

Furthermore, the as-designed numerical results seem to clearly follow the strain gradient Timoshenko theory, whereas the strain

gradient Euler-Bernoulli curve does not provide an accurate solution to the overall bending behavior. Although it should be noticed that for the thickness-to-length ratios of two thinnest specimens ($h < 5$ mm) the strain gradient beam models are already very close to each other.

Comparison between as-manufactured and as-design results

All in all, the overall stiffening tendency is similar to the one observed from the experimental and as-manufactured numerical analysis. But the as-manufactured values are about 50% higher than the designed ones as shown in Fig. 13. The as-manufactured computations always lie within the uncertainty range of the experimental measurements, whereas as-designed numerical results never fall in this range. This rather large difference has been observed in similar studies conducted by the same authors on tensile behaviors of octet-truss lattices [18].

Moreover, when a closer study on the as-manufactured and as-designed geometries is undertaken, the stiffening trend differs. Firstly, we have observed that the considered octet-truss beams experience size effects, such that classical beam theories are not applicable to approximate the bending behavior, whereas strain gradient beam theories provide a much more accurate description. Secondly, the as-manufactured bending rigidities show a stronger stiffening effect than the designed ones, as also reflected in the intrinsic material parameter determined for both geometries. This observation well correlates to all other material characteristics determined by the authors.

6. Conclusions

The numerical analysis of additively manufactured metamaterials can be prohibitively expensive and often impossible at full scale. In the present work, we have shown and validated an efficient numerical framework to incorporate complex as-manufactured geometries in a direct image-to-analysis workflow. The achieved numerical results are fully supported by the experi-

mental tests performed on the octet-truss lattices. These findings suggest that in both direct numerical simulations and beam theories there is a strong need to incorporate as-manufactured geometries into the numerical analysis of lattice structures manufactured using LPBF. In particular, the direct numerical simulation of CT-based as-manufactured geometries delivers results very close to the experimental measurements, whereas numerical analysis computed on the as-designed model fails to correctly predict the mechanical behavior of these metamaterials, presenting relative errors in the bending rigidity value always above 40%. We would like to remark that this astonishing deviation is not general to all additive manufacturing processes. Although we expect the deviations not to be so drastic for trusses with larger diameters, the manufactured octet-truss structures are already at the upper limit of the used LPBF process. Considering the majority of LPBF printers, the size of the octet-truss lattices is near the upper bound of the cell size. Larger cells would require support structures to prevent bending distortions of the struts and heat accumulation. This, in turn, introduces a practically unsurpassed level of complexity in the support removal. By contrast, when a smaller size of geometrical features is considered, the gap between as-manufactured and as-designed structures drastically increases. Thus, an accurate prediction of the mechanical properties of both small and large-scale lattices requires an incorporation of production defects into computational models.

Furthermore, we have demonstrated the applicability of classical and strain gradient beam theories to the prediction of the bending behavior of AM octet-truss lattices. This work has confirmed that size effects arise in these metamaterials, thus raising the importance of the high-order continuum theories. Additionally, we validated the strain gradient beam theories in combination with the Finite Cell Method. In particular, a high-order intrinsic material parameter was determined directly from the numerical analysis of the as-manufactured geometries. As this material parameter is independent of the problem type, it can be used for the dimensionally reduced modeling of such octet-truss lattice components under different loadings and boundary conditions.

Overall, the image-to-analysis workflow is not limited to the analysis of the bending rigidity of the metamaterials. This work serves as a step towards the complete validation of the proposed approach in application to the additive manufacturing product simulation. It can be naturally applied to the mechanical characterization of almost any type of manufactured product, e.g., to determine the linear elastic characteristics in tension or shear or thermal quantities. Furthermore, it is flexible to be extended to perform the non-linear analysis. For example, limit load could be an essential characteristic of the manufactured lattices.

To conclude, the proposed numerical framework provides an accurate and flexible tool to analyze the behavior of as-manufactured metamaterials. Furthermore, these results represent an excellent initial step toward the validation of the strain gradient continuum theories in the field of additive manufacturing. In this line of research, we intend to incorporate the demonstrated technique into the analysis of the statistically similar CT models of such mechanical metamaterials in the future. This step will then allow to expand the capabilities of the proposed image-to-material-characterization workflow. It would mainly allow evaluating the possible variability of the mechanical quantity under constant manufacturing conditions. For example, a variability of the homogenized Young's modulus can be assessed depending on the underlying lattice microstructure and fixed printing parameters. This can be done by analyzing the CT image of an as-manufactured structure and generating a set of statistically similar geometries. Thus, such an approach could evaluate the variability before the manufacturing process via sample printing. This could be especially useful to establish an expected safety factor depending on the used manufacturing parameters.

Data Availability

The raw and the processed data required to reproduce these findings cannot be shared at this time due to technical limitations. Furthermore, the data also forms part of an ongoing study.

Declaration of Competing Interest

The authors declare that they have no known competing financial interests or personal relationships that could have appeared to influence the work reported in this paper.

Acknowledgements

References

[1] A. Abedian, J. Parvizian, A. Düster, H. Khademyzadeh, E. Rank, Performance of Different Integration Schemes in Facing Discontinuities in the Finite Cell Method, Int. J. Comput. Methods 10 (03) (2013) 1350002.

[2] ASTM International, ASTM E 111–17: Standard Test Method for Young's Modulus, Tangent Modulus, and Chord Modulus, American Society for Testing and Materials, West Conshohocken, PA, 2017.

[3] X. Cao, Y. Jiang, T. Zhao, P. Wang, Y. Wang, Z. Chen, Y. Li, D. Xiao, D. Fang, Compression experiment and numerical evaluation on mechanical responses of the lattice structures with stochastic geometric defects originated from additive-manufacturing, Compos. Part B: Eng. 194 (2020) 108030.

[4] M. Dallago, B. Winiarski, F. Zanini, S. Carmignato, M. Benedetti, On the effect of geometrical imperfections and defects on the fatigue strength of cellular lattice structures additively manufactured via selective laser melting, Int. J. Fatigue 124 (2019) 348–360.

[5] V. Deshpande, N. Fleck, M. Ashby, Effective properties of the octet-truss lattice material, J. Mech. Phys. Solids 49 (8) (2001) 1747–1769.

[6] A. du Plessis, I. Yadroitsava, I. Yadroitsev, Effects of defects on mechanical properties in metal additive manufacturing: A review focusing on x-ray tomography insights, Mater. Des. 187 (2020) 108385.

[7] A. Düster, E. Rank, B.A. Szabó, The p-version of the finite element method and finite cell methods, in: E. Stein, R. Borst, T.J.R. Hughes (Eds.), Encyclopedia of Computational Mechanics, vol. 2, John Wiley & Sons, Chichester, West Sussex, 2017, pp. 1–35.

[8] I. Echeta, B. Dutton, X. Feng, R. Leach, S. Piano, Review of defects in lattice structures manufactured by powder bed fusion, Int. J. Adv. Manuf. Technol. 106 (2020) 2649–2668.

[9] M. Elhaddad, N. Zander, T. Bog, L. Kudela, S. Kollmannsberger, J.S. Kirschke, T. Baum, M. Ruess, E. Rank, Multi-level hp-finite cell method for embedded interface problems with application in biomechanics, Int. J. Numer. Methods Biomed. Eng. 34 (4) (2018) e2951.

[10] M. Elhaddad, N. Zander, S. Kollmannsberger, A. Shadavakhsh, V. Nübel, E. Rank, Finite Cell Method: High-Order Structural Dynamics for Complex Geometries, Int. J. Struct. Stab. Dyn. 15 (7) (2015) 1540018.

[11] J. Haubrich, J. Gussone, P. Barriobero-Vila, P. Kürnsteiner, E.A. Jägle, D. Raabe, N. Schell, G. Requena, The role of lattice defects, element partitioning and intrinsic heat effects on the microstructure in selective laser melted Ti-6Al-4V, Acta Mater. 167 (2019) 136–148.

[12] Y. Hua, D. Timofeev, I. Giorgio, W. Mueller, Effective strain gradient continuum model of metamaterials and size effects analysis, Continuum Mech. Thermodyn. (2020).

[13] Joint Committee for Guides in Metrology, JCGM 100: Evaluation of Measurement Data - Guide to the Expression of Uncertainty in Measurement, 2008.

[14] J. Jomo, N. Zander, M. Elhaddad, A.I. Özcan, S. Kollmannsberger, R.-P. Mundani, E. Rank, Parallelization of the multi-level hp-adaptive finite cell method, Comput. Math. Appl. 74 (1) (2017) 126–142.

[15] J.N. Jomo, F. de Prenter, M. Elhaddad, D. D'Angella, C.V. Verhoosel, S. Kollmannsberger, J.S. Kirschke, V. Nübel, E.H. van Brummelen, E. Rank, Robust and parallel scalable iterative solutions for large-scale finite cell analyses, Finite Elem. Anal. Des. 163 (2019) 14–30.

[16] S. Khakalo, V. Balobanov, J. Niiranen, Modelling size-dependent bending, buckling and vibrations of 2D triangular lattices by strain gradient elasticity models: Applications to sandwich beams and auxetics, Int. J. Eng. Sci. 127 (2018) 33–52.

[17] S. Khakalo, J. Niiranen, Lattice structures as thermoelastic strain gradient metamaterials: Evidence from full-field simulations and applications to functionally step-wise-graded beams, Compos. Part B: Eng. 177 (2019) 107224.

[18] N. Korshunova, G. Alaimo, S. Hosseini, M. Carraturo, A. Reali, J. Niiranen, F. Auricchio, E. Rank, S. Kollmannsberger, Image-based numerical characterization and experimental validation of tensile behavior of octet-truss lattice structures, Additive Manuf. 41 (2021) 101949.

[19] N. Korshunova, J. Jomo, G. Lékó, D. Reznik, P. Balázs, S. Kollmannsberger, Image-based material characterization of complex microarchitectured additively manufactured structures, Comput. Math. Appl. 80 (11) (2020) 2462–2480.

[20] L. Kudela, N. Zander, S. Kollmannsberger, E. Rank, Smart octrees: Accurately integrating discontinuous functions in 3D, Comput. Methods Appl. Mech. Eng. 306 (2016) 406–426.

[21] R.M. Latture, M.R. Begley, F.W. Zok, Design and mechanical properties of elastically isotropic trusses, J. Mater. Res. 33 (3) (2018) 249–263.

[22] H. Lei, C. Li, J. Meng, H. Zhou, Y. Liu, X. Zhang, P. Wang, D. Fang, Evaluation of compressive properties of SLM-fabricated multi-layer lattice structures by experimental test and μ-CT-based finite element analysis, Mater. Des. 169 (2019) 107685.

[23] L. Liu, P. Kamm, F. García-Moreno, J. Banhart, D. Pasini, Elastic and failure response of imperfect three-dimensional metallic lattices: The role of geometric defects induced by Selective Laser Melting, J. Mech. Phys. Solids 107 (2017) 160–184.

[24] B. Lozanovski, M. Leary, P. Tran, D. Shidid, M. Qian, P. Choong, M. Brandt, Computational modelling of strut defects in SLM manufactured lattice structures, Mater. Des. 171 (2019) 107671.

[25] T. Maconachie, M. Leary, B. Lozanovski, X. Zhang, M. Qian, O. Faruque, M. Brandt, SLM lattice structures: Properties, performance, applications and challenges, Mater. Des. 183 (2019) 108137.

[26] R. Mindlin, N. Eshel, On first strain-gradient theories in linear elasticity, Int. J. Solids Struct. 4 (1) (1968) 109–124.

[27] J. Niiranen, V. Balobanov, J. Kiendl, S. Hosseini, Variational formulations, model comparisons and numerical methods for Euler-Bernoulli micro- and nano-beam models, Math. Mech. Solids 24 (1) (2019) 312–335.

[28] A. Norouzi, M.S.M. Rahim, A. Altameem, T. Saba, A.E. Rad, A. Rehman, M. Uddin, Medical image segmentation methods, algorithms, and applications, IETE Tech. Rev. 31 (3) (2014) 199–213.

[29] M. O'Masta, L. Dong, L. St-Pierre, H. Wadley, V. Deshpande, The fracture toughness of octet-truss lattices, J. Mech. Phys. Solids 98 (2017) 271–289.

[30] P. Onck, E. Andrews, L. Gibson, Size effects in ductile cellular solids. Part I: modeling, Int. J. Mech. Sci. 43 (3) (2001) 681–699.

[31] J. Parvizian, A. Düster, E. Rank, Finite cell method, Comput. Mech. 41 (1) (2007) 121–133.

[32] M. Rashed, M. Ashraf, R. Mines, P.J. Hazell, Metallic microlattice materials: A current state of the art on manufacturing, mechanical properties and applications, Mater. Des. 95 (2016) 518–533.

[33] Renishaw-PLC, Data sheet: SS 316L-0407 powder for additive manufacturing. Renishaw-PLC, 2020.

[34] T.A. Schaedler, W.B. Carter, Architected cellular materials, Annu. Rev. Mater. Res. 46 (1) (2016) 187–210.

[35] Y. Sha, L. Jiani, C. Haoyu, R.O. Ritchie, X. Jun, Design and strengthening mechanisms in hierarchical architected materials processed using additive manufacturing, Int. J. Mech. Sci. 149 (2018) 150–163.

[36] S. Tahaei Yaghoubi, V. Balobanov, S.M. Mousavi, J. Niiranen, Variational formulations and isogeometric analysis for the dynamics of anisotropic gradient-elastic euler-bernoulli and shear-deformable beams, Eur. J. Mech. A. Solids 69 (2018) 113–123.

[37] T. Tancogne-Dejean, D. Mohr, Elastically-isotropic truss lattice materials of reduced plastic anisotropy, Int. J. Solids Struct. 138 (2018) 24–39.

[38] H.-T. Thai, T.P. Vo, T.-K. Nguyen, S.-E. Kim, A review of continuum mechanics models for size-dependent analysis of beams and plates, Compos. Struct. 177 (2017) 196–219.

[39] J. Torabi, R. Ansari, M. Darvizeh, A c1 continuous hexahedral element for nonlinear vibration analysis of nano-plates with circular cutout based on 3d strain gradient theory, Compos. Struct. 205 (2018) 69–85.

[40] J. Torabi, R. Ansari, M. Darvizeh, Application of a non-conforming tetrahedral element in the context of the three-dimensional strain gradient elasticity, Comput. Methods Appl. Mech. Eng. 344 (2019) 1124–1143.

[41] J. Torabi, J. Niiranen, R. Ansari, Nonlinear finite element analysis within strain gradient elasticity: Reissner-mindlin plate theory versus three-dimensional theory, Eur. J. Mech. A. Solids 87 (2021) 104221.

[42] B. Vayssette, N. Saintier, C. Brugger, M. El May, E. Pessard, Numerical modelling of surface roughness effect on the fatigue behavior of Ti-6Al-4V obtained by additive manufacturing, Int. J. Fatigue 123 (2019) 180–195.

[43] C. Yan, L. Hao, A. Hussein, D. Raymont, Evaluations of cellular lattice structures manufactured using selective laser melting, Int. J. Mach. Tools Manuf 62 (2012) 32–38.

[44] Z. Yang, S. Kollmannsberger, A. Düster, M. Ruess, E.G. Garcia, R. Burgkart, E. Rank, Non-standard bone simulation: Interactive numerical analysis by computational steering, Comput. Vis. Sci. 14 (5) (2012) 207–216.

[45] Z. Yang, M. Ruess, S. Kollmannsberger, A. Düster, E. Rank, An efficient integration technique for the voxel-based finite cell method, Int. J. Numer. Meth. Eng. 91 (5) (2012) 457–471.

[46] M. Yoder, L. Thompson, J. Summers, Size effects in lattice structures and a comparison to micropolar elasticity, Int. J. Solids Struct. 143 (2018) 245–261.

[47] X. Zheng, H. Lee, T.H. Weisgraber, M. Shusteff, J. DeOtte, E.B. Duoss, J.D. Kuntz, M.M. Biener, Q. Ge, J.A. Jackson, S.O. Kucheyev, N.X. Fang, C.M. Spadaccini, Ultralight, ultrastiff mechanical metamaterials, Science 344 (6190) (2014) 1373–1377.